Inhibitor and NAD^+ Binding to Poly(ADP-ribose) Polymerase As Derived from Crystal Structures and Homology Modeling[†,‡]

Armin Ruf,[§] Gilbert de Murcia,[||] and Georg E. Schulz*[,§]

Institut für Organische Chemie und Biochemie, Albertstrasse 21, D-79104 Freiburg im Breisgau, Germany, and École Supérieure de Biotechnologie de Strasbourg, UPR 9003 du CNRS, Boulevard Sébastien Brant, F-67400 Illkirch-Graffenstaden, France

Received September 26, 1997; Revised Manuscript Received December 18, 1997

ABSTRACT: Inhibitors of poly(ADP-ribose) polymerase (PARP, EC 2.4.2.30) are of clinical interest because they have potential for improving radiation therapy and chemotherapy of cancer. The refined binding structures of four such inhibitors are reported together with the refined structure of the unligated catalytic fragment of the enzyme. Following their design, all inhibitors bind at the position of the nicotinamide moiety of the substrate NAD^+. The observed binding mode suggests inhibitor improvements that avoid other NAD^+-binding enzymes. Because the binding pocket of NAD^+ has been strongly conserved during evolution, the homology with ADP-ribosylating bacterial toxins could be used to extend the bound nicotinamide, which is marked by the inhibitors, to the full NAD^+ molecule.

Poly(ADP-ribose) polymerase (PARP,[1] EC 2.4.2.30) is located in the nucleus of most eukaryotes and helps to maintain genomic integrity in base excision repair (*1*), in DNA recombination (*2*), and in cellular differentiation (*3*). Moreover, it participates in chromatin organization (*4*). PARP is activated by binding to DNA strand breaks (*5*). It modifies numerous nuclear proteins such as histones, proteins of the replication machinery, and also PARP itself by initial ADP-ribosylation as well as subsequent elongation and branching (every 40−50 units) of the protein-attached ADP-ribose chain. The catalyzed reaction is $NAD^+ + X \rightarrow$ ADP-5′-ribose-1′-X + nicotinamide, where the acceptor X is a glutamate of a protein (initiation), the 2′-hydroxyl of the terminal adenine ribose of poly(ADP-ribose) (elongation), or the 2′-hydroxyl of a nicotinamide ribose of the polymer (branching). The modified proteins lose their affinity to DNA and provide space for DNA repair. PARP is a potential antitumor drug target because its inhibitors potentiate the cytotoxic effects of radiation and of monofunctional alkylating agents used in cancer therapy (*6, 7*).

Human PARP consists of 1014 residues organized in three functionally distinct parts: an N-terminal DNA-binding region, a central regulatory region, and a C-terminal region carrying the ADP ribosyltransferase (ARTase) activity (*5*). The C-terminal region keeps the basal activity of nonactivated PARP, which is 0.2% of the maximum (*8*). The structure of a C-terminal catalytic fragment of the PARP from chicken (PARP-CF) is known (*9*). It is structurally homologous to the catalytic domains of bacterial ADP-ribosylating toxins (*9*). Presumably, the family also comprises other known ARTases (*10*). Here we report the refined crystal structure of unligated PARP-CF from chicken at 2.3 Å resolution together with the structures of four specific PARP inhibitor complexes at resolutions of 2.4−2.8 Å. Furthermore, the binding mode of NAD^+ is deduced from the nicotinamide position marked by the inhibitors in conjunction with homology modeling based on a toxin complex (*11*).

MATERIALS AND METHODS

Crystal Production and Data Collection. PARP-CF was produced and crystallized as described (*12*). The structure of the unligated enzyme was established by multiple isomorphous replacement at 2.5 Å resolution (*9*). A new data set was then collected to 2.3 Å resolution using synchrotron radiation (beamlines X11 and BW7B with image plates; EMBL outstation, Hamburg) and processed with MOSFLM (*13*) and SCALA (*14*). Furthermore, three crystals of inhibitor complexes were produced by cocrystallizing with 0.03 mM 4-amino-1,8-naphthalimide (4ANI), 5 mM 3-methoxybenzamide (3MBA), and 10 mM 8-hydroxy-2-methyl-3-hydroquinazolin-4-one (NU1025), respectively. The X-ray data from these crystals were collected at a synchrotron (beamline X31 with image plate; EMBL outstation, Hamburg) and processed with DENZO and SCALEPACK (*15*). The data from a fourth inhibitor complex [cocrystals with 1.8 mM 3,4-dihydro-5-methylisoquinolinone, PD128763 (*9*)] were refined. The inhibitor structures are depicted in Figure 1.

[†] This work was supported by the Deutsche Forschungsgemeinschaft under SFB-388 and by the Association pour la Recherche contre le Cancer.

[‡] The coordinates and structure factors are deposited in the Protein Data Bank under codes 2PAW, 1PAX, 2PAX, 3PAX, and 4PAX.

* Corresponding author: Phone: +49-761-203-6058. Fax: +49-761-203-6161. E-mail: schulz@bio5.chemie.uni-freiburg.de.

[§] Institut für Organische Chemie und Biochemie.

[||] École Supérieure de Biotechnologie de Strasbourg.

[1] Abbreviations: 3MBA, 3-methoxybenzamide; 4ANI, 4-amino-1,8-naphthalimide; ARTase, adenosine 5′-diphosphate ribosyltransferase; DT, diphtheria toxin; NMN, nicotinamide mononucleotide (β-nicotinamide ribose 5′-phosphate); NU1025, 8-hydroxy-2-methyl-3-hydroquinazolin-4-one; PARP, poly(ADP-ribose) polymerase; PARP-CF, catalytic fragment of PARP; PD128763, 3,4-dihydro-5-methylisoquinolinone.

S0006-2960(97)02383-0 CCC: $15.00
Published on Web 02/26/1998

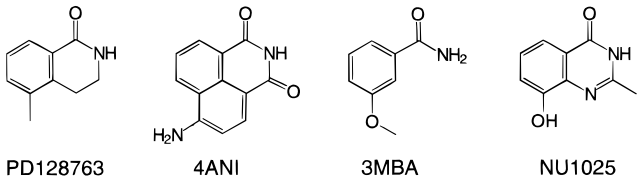

FIGURE 1: Covalent structures of the four applied inhibitors. See Figure 4 for details.

Structure Determination and Refinement. The structure of complex PARP-CF:PD128763 (*9*) was refined to completion, using X-PLOR with bulk solvent correction (*16*, *17*) and adding further water molecules. The resulting peptide structure was taken as the starting model for all other structures reported here.

For the refinement of the three other inhibitor complexes, we started with the polypeptide and the water molecules of complex PARP-CF:PD128763 and added the respective inhibitor. Topology and parameter files of the inhibitors were produced with XPLO2D (*18*) from models created with SYBYL (*19*). The resulting models were then subjected to positional and *B*-factor refinements in X-PLOR using the bulk solvent correction. For complex PARP-CF:NU1025 only an overall *B*-factor was refined.

For the refinement of unligated PARP-CF, we started with the polypeptide of PARP-CF:PD128763 and used X-PLOR with the bulk solvent correction (*16*, *17*). Water molecules were added according to the emerging electron densities. R_{free} was used throughout as a guide (*20*). The last refinement round included all measured reflections. Although the backbone electron density remained discontinuous for residues 783−786, 824−825, and 827, all of them were included with high *B*-factors.

Modeling of Bound NAD$^+$. Two rotation/translation operators were obtained by superimposing residues involved in NAD^+ binding in diphtheria toxin (*11*) onto the corresponding residues of PARP-CF. For this purpose NAD^+ was subdivided into the nicotinamide (NMN) and adenine (AMP) moieties, both including the phosphate-bridging O3 atom. The first operator was based on the C^α atoms of the 7 residues with atoms closer than 4 Å to NMN, and the second operator, on the respective 12 C^α atoms at the AMP moiety. Using these operators, NAD^+ as bound to diphtheria toxin was transferred in two pieces to PARP-CF and there reconnected by placing a new O3 atom at the center of the two O3 positions of the pieces. This model was then relaxed by 200 cycles of conjugate gradient energy minimization using X-PLOR (*16*) and keeping the polypeptide fixed. The nicotinamide was positionally restrained to the corresponding atoms of the inhibitors (average of three inhibitors; NU1025 was omitted because of inferior resolution), and the ribose puckers were restrained to those observed in the diphtheria toxin complex (*11*).

RESULTS AND DISCUSSION

Structure Analysis. All crystals were isomorphous with those analyzed before (*9*, *12*). The reported structure of PARP-CF is from chicken, but it shows 87% sequence identity with the respective human fragment that is the drug target. All stated sequence numbers are for the human enzyme (subtract 3 to obtain chicken numbers). All crystallized peptides comprise residues 654−1014, whereas the reported structures include only residues 662−1009 for unligated PARP-CF and residues 662−1011 for the inhibitor complexes. The first eight and the last three (unligated: five) residues could not be located in the electron density and are most likely mobile. An overview of the structure is given in Figure 2.

Using the newly collected X-ray data (Table 1), the structure of the unligated enzyme was improved in detail when compared to the published model (*9*). With higher resolution, the *B*-factor distribution became more pronounced and the number of water molecules doubled (Table 2). The largest shifts of C^α atoms were 1.5 Å, but all shifts above 0.5 Å occurred in regions with high *B*-factors. The *R*-factor and R_{free} dropped, and more indicative, the Ramachandran quality (*21*) improved from 87% to 92% of the residues being in most favored regions.

The structure of complex PARP-CF:PD128763 was improved by refinement. The *R*-factor and R_{free} dropped from 21.2% and 31.2% (*9*) to the rather low values of 16.9% and 24.4%, respectively. The Ramachandran quality (*21*) increased from 89% to 92% of the residues being in most favored regions.

The resulting *B*-factor distributions are depicted in Figure 3 together with the C^α distances between unligated PARP-CF and its complex with inhibitor PD128763. The C^α shifts are below 1.1 Å and occur mostly in the mobile regions and not around the inhibitor. Remarkable is the structural solidification around residue 908 at the bound inhibitor. The respective data of the other inhibitors are similar.

At the packing contacts, crystal structures tend to deviate slightly from the structure in solution. Therefore, we listed all of these contacts in Table 3. On crystallization, 25% of the surface area of PARP-CF is buried in the contacts.

Domain Organization. PARP-CF is monomeric and can be subdivided into two domains (Figure 2). The N-terminal domain (residues 662−784) consists of five α-helixes and one 3_{10}-helix (Figure 3). A search with program DALI (*22*) failed to show a significant structural similarity with other domains in the Protein Data Bank. The C-terminal domain (residues 785−1014) belongs to the family of ARTases as derived from chain fold similarities (*9*). PARP is a special family member because it mono-ADP-ribosylates a protein (initiation) like the other ARTases, but it then elongates this modification to a polymer. All other structurally known family members are bacterial toxins (*23*−*27*).

Although the C-terminal domain of PARP-CF is homologous to the toxins, it cannot be expressed in a functional form. The smallest fragment that retains the basal activity of the nonactivated full enzyme has been found to start at residue 654, comprising both domains (*28*). This observation finds an explanation in the structure, because there is a hydrophobic core shared between the C-terminal domain and helix A (residues 667−676) of the N-terminal domain. The C-terminal domain is destabilized by removing helix A because this core is broken up and numerous hydrophobic residues are exposed to the solvent.

Inhibitor Binding. PARP inhibitors are of clinical interest (see above). Most of them are isosteric to the nicotinamide moiety of NAD^+ (Figure 1). We established the interactions of three such nicotinamide analogues with PARP-CF. Moreover, the complex structure of a fourth inhibitor, PD128763, was improved. The data on the inhibitor

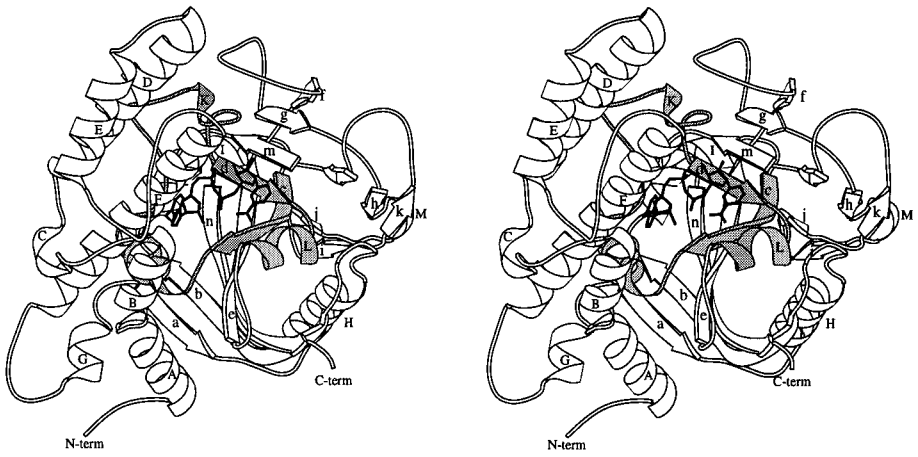

FIGURE 2: Ribbon representation of PARP-CF *(36)*. Secondary structure elements are labeled according to Ruf et al. *(9)*. A sequence motif strongly conserved within all PARP species (residues 859−908) is marked in gray. It participates in NAD+ binding as demonstrated by the modeled NAD+ (black).

Table 1: Data Collection with Unligated and Ligated PARP-CF (Last Shell Values in Parentheses)

data set	unligated	PD128763[a]	4ANI	3MBA	NU1025
resolution (Å)	28−2.3 (2.36−2.30)	12−2.4 (2.44−2.40)	15−2.4 (2.44−2.40)	20−2.4 (2.42−2.40)	15−2.8 (2.89−2.80)
wavelength (Å)	0.87/0.93	0.92	0.92	0.98	0.92
completeness (%)	94 (98)	99 (94)	95 (73)	99 (100)	100 (100)
R_{merge} (%)[b]	12.8[c] (28.2)[c]	7.3 (28.2)	7.3 (23.2)	7.2 (39.4)	7.5 (26.8)
redundancy	4.1 (3.9)	4.5 (2.8)	3.7 (2.7)	3.7 (3.7)	4.4 (4.4)
average I/σ	4.6[c] (2.5)[c]	11.5 (4.2)	13.8 (7.3)	9.7 (3.2)	10.5 (7.7)
collected data	63555 (4665)	68037 (1936)	49815 (1411)	56084 (2729)	40520 (3180)
unique data	15604 (1194)	14941 (692)	13590 (530)	15091 (730)	9296 (724)
B-factor (Å^2)[d]	32	40	40	37	39

[a] The data are given for reference; they have already been published *(9)*. [b] $R_{merge} = \sum_h\sum_i|I(h)_i - \langle I(h)\rangle|/\sum_h\sum_i I(h)_i$. [c] The native data set was collected from two isomorphous crystals at two different wavelengths. Merging and scaling these sets resulted in a rather low average I/σ value, although the respective individual values were high. We suggest that merging such data is still the best procedure to diminish the systematic errors, despite its adverse effects on the average I/σ and on R_{merge}. [d] Derived from Wilson plots.

Table 2: Refinement Statistics[a]

structure	unligated	PD128763	4ANI	3MBA	NU1025
resolution range (Å)	28−2.3	12−2.4	15−2.4	20−2.4	15−2.8
no. of reflections	15604	14941	13590	15091	9296
R-factor (%)	19.4	16.9	16.7	17.1	16.7
R_{free} (%)[b]	26.8	24.4			
no. of atoms, total	2842	2858	2853	2850	2830
protein	2747[c]	2763	2763	2763	2763
inhibitor		12	16	11	13
water	95	83	74	76	54
coordinate error (Å)[d]	0.29	0.29	0.30	0.29	0.32
mean B-factors, protein	35	35	36	35	31[e]
ligand		19	40	22	18[e]
water	43	42	41	40	35[e]
Ramachandran quality (%)[f]	92	92	92	92	92

[a] All measured reflections were used, giving rise to a variety of low-resolution limits. The X-PLOR bulk solvent correction *(17)* was applied. For all structures the rms deviations from standard geometry are 0.010 Å for bond lengths and 1.5° for bond angles. The rms deviations of B-factors along a bond are in the range 2.3−2.8 Å^2 (4.2−4.8 Å^2) for main (side) chain atoms. Those along an angle are 3.7−4.4 Å^2 (6.6−7.3 Å^2). [b] R_{free} was calculated for a 10% random subset of the data *(20)*. [c] Residues 1010−1011 are missing when compared with the others. [d] According to *(35)*, using data from 5.0 Å to the resolution limit. [e] The B-factor distribution was taken from the PD128763 model, and only the overall B-factor was refined. [f] Residues located in most favored regions *(21)*. There is no residue in a disallowed region.

complexes are given in Tables 1 and 2. The electron densities are depicted in Figure 4.

In all cases the ligated polypeptides do not differ substantially from the unligated structure. The rms deviations of the C^α atoms range between 0.22 and 0.27 Å. Only the surface loop (residues 823−827) between helix H and β-strand b moves significantly, by about 1 Å (Figure 3), toward the protein center, packing more tightly against helix *L* (Figure 2). Two segments of PARP-CF become more ordered upon inhibitor binding: a segment including helix L (residues 901−910) that carries the inhibitor binding residues Ser904 and Tyr907, and the surface loop 823−827 mentioned above (Figure 3).

As designed, all inhibitors bind to the well-defined nicotinamide subsite of the NAD+-binding pocket (Figure 4). Common to all inhibitor complexes are the hydrogen bonds between Gly863-N, Gly863−O, and Ser904-OG on one side and the inhibitor amide or lactame group on the

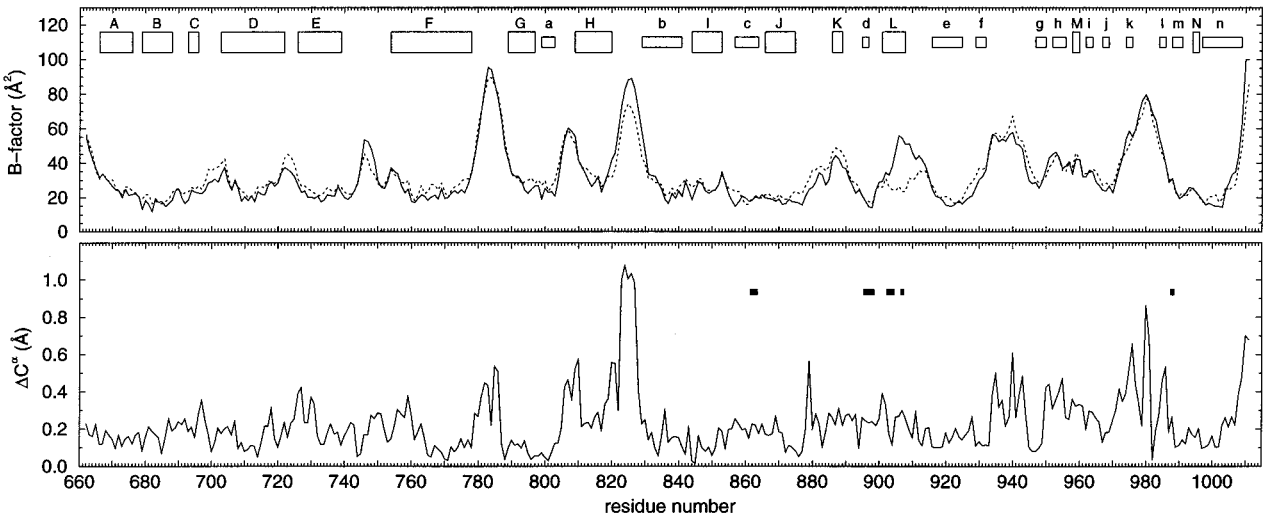

FIGURE 3: Chain mobilities and shifts. Top: *B*-factor distributions of unligated (—) and PD128763-ligated (- - -) PARP-CF. The secondary structures depicted in Figure 2 are specified. Bottom: Distribution of C^{α} atom shifts on binding inhibitor PD128763. The respective plots for the three other inhibitor complexes are similar. The residues with atoms closer than 4 Å to the inhibitor are marked as black bars.

Table 3: Crystal Contacts of PARP-CF

contact	contact area[a] (Å²)	involved residues[b]	no. of hydrogen bonds
I	910	a−b_1	7
	910	b−a_2	7
II	480	c−d_3	4
	480	d−c_4	4
III	380	e−f_5	3
	380	f−e_6	3
IV	280	g−h_7	3
	280	h−g_8	3

[a] The solvent-accessible area of the reference molecule buried in the crystal contact as calculated with X-PLOR (probe radius 1.4 Å). The total solvent-accessible surface of PARP-CF is 16278 Å². [b] Residues whose solvent-accessible surface decreases by more than 1 Å² on packing. A minor contact between residues 667 and 722 has been neglected. The reference molecule at [*x*, *y*, *z*] is in contact with eight symmetry-related molecules: 1, S4 + (0, 0, 0); 2, S4 + (−1, 0, 0); 3, S2 + (1, 1, 0); 4, S2 + (1, 1, −1); 5, S3 + (2, 0, 0); 6, S3 + (2, −1, 0); 7, S3 + (1, 0, 0); and 8, S3 + (1, −1, 0), where S2 = [$^1/_2 - x$, $-y$, $^1/_2 + z$], S3 = [$-x$, $^1/_2 + y$, $^1/_2 - z$], and S4 = [$^1/_2 + x$, $^1/_2 - y$, $-z$] are the symmetry operators. Residue lists: a = 692, 695, 700, 725−727, 730, 734, 737−738, 741−751, 753; b = 668, 671, 675, 678, 680−681, 683−684, 687−688, 690, 693−694, 743, 745, 834, 866, 911−916, 1004, 1006, 1008−1012; c = 679, 683, 693−695, 697−700, 775, 779, 782−785; d = 852−857, 928, 931, 933, 951, 958, 961, 963, 965−966, 968, 977−979; e = 819, 822, 827, 830, 832, 957, 959, 973, 975, 1008−1012; f = 664, 787, 800, 802, 809−810, 813, 838, 840, 849, 962−966; g = 720−724, 726, 729, 753, 755, 980−981; h = 707, 846, 849, 850, 852−853, 883.

other. The more potent inhibitors PD128763, 4ANI, and NU1025 have the amide group fixed in a heteroring (Figure 1). A superposition of the polypeptides in Figure 5 demonstrates that the positional differences between the inhibitors are small. Omitting NU1025 because of inferior resolution, the respective atoms have been averaged to yield the nicotinamide position. The nicotinamide-binding pocket is lined by residues 862−863, 896−898, 903−904, 907, and 988 (at least one atom at a distance below 4 Å).

3MBA and 3-aminobenzamide are widely used inhibitors in PARP research and serve as references for new inhibitors. Both have a rotable amide group lowering their affinity for entropic reasons. Moreover, 3MBA does not interact as extensively as the bi- and tricyclic inhibitors with Tyr896 and Tyr907 forming the walls of the nicotinamide-binding pocket. The latter inhibitors have lower IC_{50} values, but they also show low solubility (especially PD128763 and 4ANI), limiting their usefulness. The solvent-accessible protein surfaces covered by PD128763, 4ANI, 3MBA, NU1025 and nicotinamide are 119, 144, 115, 127, and 96 Å², respectively.

Although not designed to do so, 4ANI and NU1025 form additional hydrogen bonds to the polar side chain atoms of Glu988 and Tyr907, respectively. On the basis of the observed structures, inhibitors can now be modified to interact even more favorably with the polypeptide. A carboxamide group, for instance, could be attached to the 5-methyl group of PD128763 (Figure 1) for hydrogen bonding to Lys903-NZ, Tyr907-OH, and Glu988-OE2. This should increase the specificity as well as the solubility of this inhibitor.

NAD^+ Binding. In numerous experiments we tried to bind NAD^+ and analogues in PARP-CF crystals by soaking with and without subsequent flash freezing and by cocrystallizations. In none of our attempts did we find a bound ADP-ribose moiety of NAD^+. Fortunately, there are two ligated homologous structures, from which the location of this part can be deduced. The binding site of the NAD^+ analogue β-methylenethiazole-4-carboxamide adenine dinucleotide is known for exotoxin A from *Pseudomonas aeruginosa* (*27*), and two crystallographically independent NAD^+ sites are known for diphtheria toxin (DT) (*11*). The two binding structures resemble each other closely. We used only the structure of complex DT:NAD^+ because it appears to be closer to the natural situation.

The cores of the catalytic domains of four ADP-ribosylating bacterial toxins (*23*−*25*, *27*) have previously been superimposed on PARP-CF, aligning 44−59 residues within a 3.0-Å cutoff (*9*). For DT this alignment left the residues binding to the adenine moiety of NAD^+ outside the 3-Å cutoff. Therefore, we did a local structural alignment based on the 17 residues with one atom closer than 4 Å to the NAD^+ molecule in complex DT:NAD^+ (*11*), seven of which are conserved in PARP (Figure 6). For modeling NAD^+ bound to PARP-CF, we split NAD^+ into two parts and transferred them separately as described in the Materials and

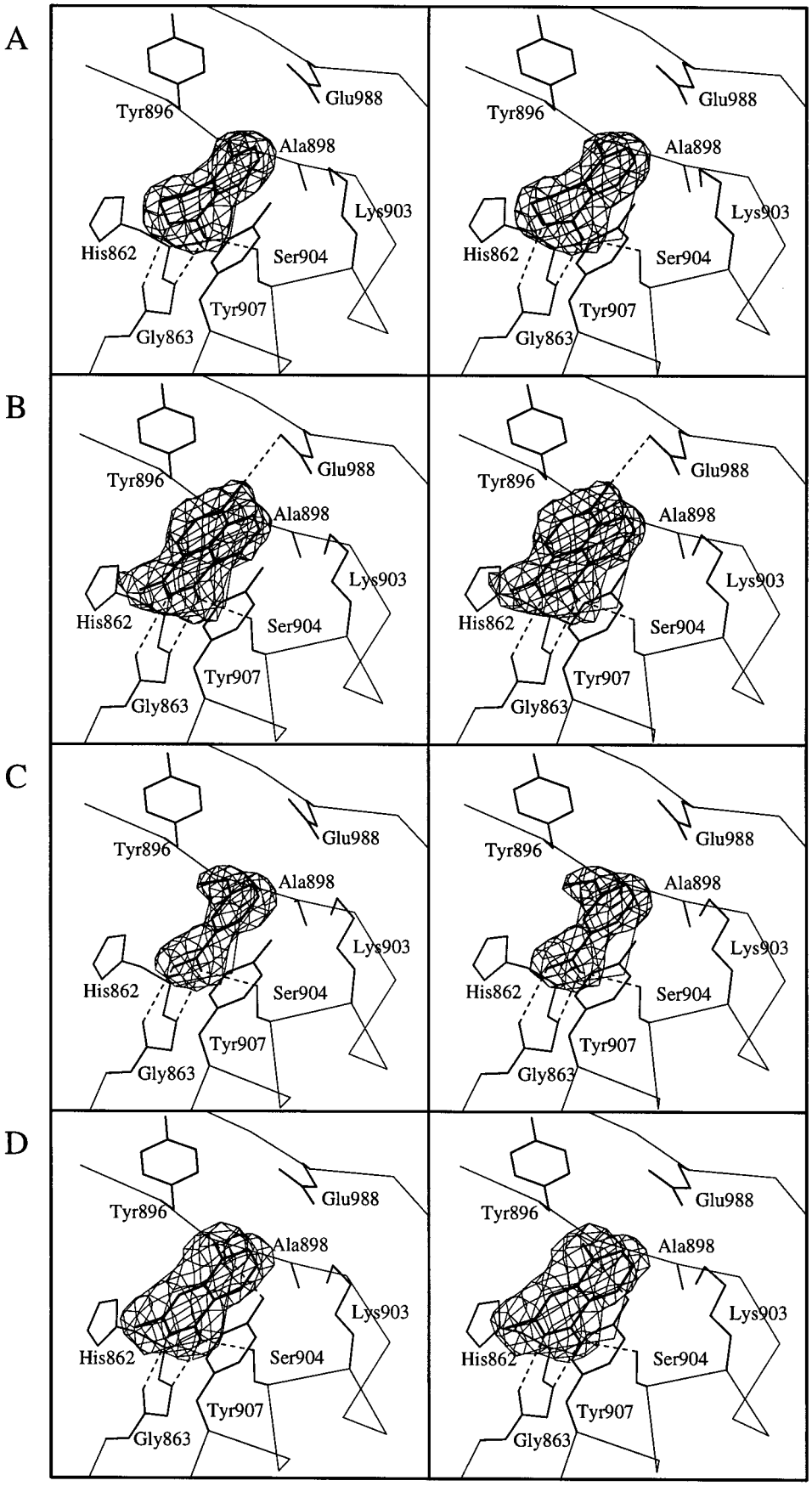

FIGURE 4: Inhibitor binding to PARP-CF. For each structure the observed ($2F_o - F_c$) electron density of the inhibitor was contoured at 1σ. All inhibitors mimick nicotinamide and actually bind in the nicotinamide-binding pocket of the enzyme. A: PD128763 ($IC_{50} = 0.16\ \mu M$) *(37)*. B: 4ANI ($IC_{50} = 0.18\ \mu M$) *(38)*. C: 3MBA ($IC_{50} = 10\ \mu M$) *(38)*. D: NU1025 ($IC_{50} = 0.4\ \mu M$) *(39)*.

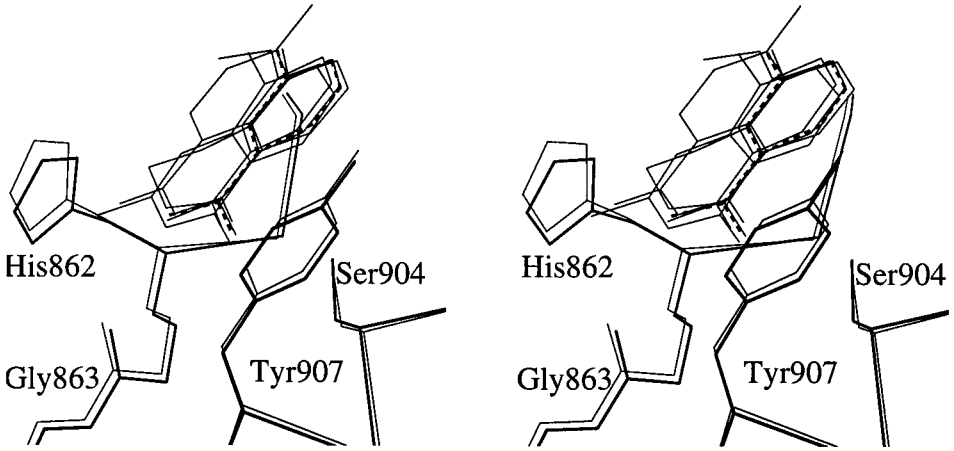

FIGURE 5: Superposition of all four inhibitors as based on the polypeptide. The neighboring residues of unligated (thin lines) and 4ANI-ligated (thick lines) PARP-CF are given. The average position of nicotinamide is marked (dashed lines). NU1025 was excluded from averaging because of inferior resolution. The resulting nicotinamide was used in homology modeling of bound NAD^+.

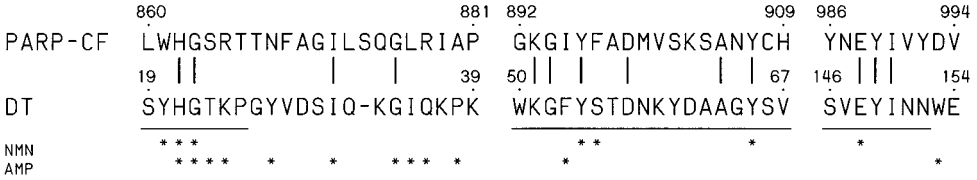

FIGURE 6: Sequence alignment of DT with PARP-CF. Conserved residues are marked by vertical bars. The underlined residues are within the 3-Å cutoff of the homologous chain folds *(9)*. For the transfer to PARP-CF, the 17 residues involved in NAD^+-binding in DT (*) were separated into 7 at the NMN moiety and 12 at the AMP moiety of NAD^+.

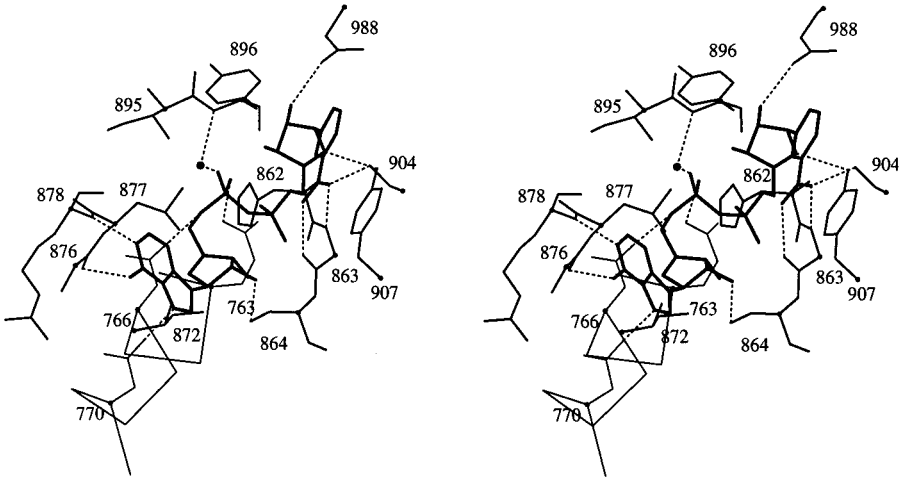

FIGURE 7: Stereoview of modeled NAD^+ as bound to PARP-CF. Putative hydrogen bonds are given (dashed lines). The NAD^+ model is based on the nicotinamide position marked by the inhibitors and on homologous binding of the ADP-ribose moiety to diphtheria toxin *(11)*, which corresponds to the ADP-ribose moiety binding to *Pseudomonas aeruginosa* exotoxin A *(27)*. The water molecule is also present in complex DT:NAD^+. See Figure 8 for the residue types. C^α atoms are marked by dots.

Methods. In the subsequent conformational refinement we applied the experimental information on the nicotinamide position marked by the inhibitors (Figure 5). The final model is depicted in Figures 7 and 8. The putative interactions are listed in Table 4. The adenine moiety is deeply buried and fixed by specific hydrogen bonds and by hydrophobic interactions. The pocket leaves some space for water molecules.

The resulting model shows internal steric strain at the adenosine ribose that appears to be more serious than the strain observed in DT:NAD^+ (*11*). This additional strain is in agreement with our failure to bind NAD^+ in crystallized PARP-CF. Because the strain is relieved on ADP-ribose transfer, it has been suggested that this strain helps in driving the reaction (*11*). The modeled NAD^+ conformation is more compact than in DT:NAD^+ (the C1′−C1′ distance is 9.6 Å, versus 11.0 Å at an rms deviation of 1.4 Å for all atoms). It is much more compact than in dehydrogenases and related enzymes (*29*).

The NAD^+ model is further supported by random mutagenesis studies searching for PARP with reduced activity. Among the observed mutants, five showed exchanges at the modeled NAD^+ (one atom closer than 4 Å), namely, N868S, L877P, F897S, F897Y, and E988K, with 4, 2.5, 10, 25, and 1.3% of wild-type activity, respectively (*30*). Four further mutations concerned nearby residues, namely, F869S, G871R, C908R and Y989H, with 25, 18, 0.5, and 65%, respectively (*30*).

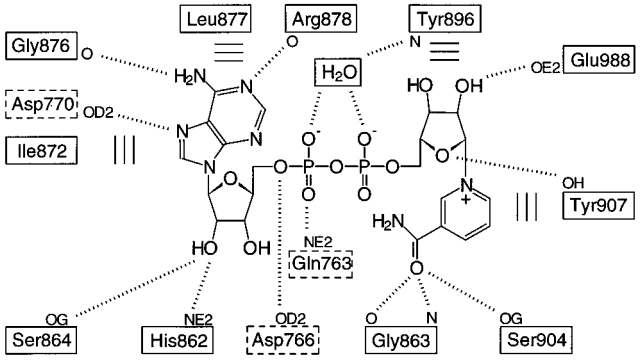

FIGURE 8: Schematic drawing of hydrogen bonds (dotted lines) and hydrophobic contacts (parallel lines) to the NAD^+ model. Dashed-line boxes are used for residues from the N-terminal domain. In the homologous complex DT:NAD^+ the phosphates are hydrogen bonded to water molecules, one of which is also present in unligated PARP-CF and depicted here.

Table 4: Polar Interactions of the Modeled NAD^+ [a]

NAD^+ atom	protein atom	distance (Å)	NAD^+ atom	protein atom	distance (Å)
$N6_A$	876-O	3.0	$O1P_N$	Wat9	3.6
$N7_A$	Asp770-OD2	2.5	$N7_N$	863-O	2.9
$N1_A$	878-N	2.7	$O7_N$	863-N	2.7
$O2'_A$	Ser864-OG	2.8	$O7_N$	Ser904-OG	2.7
$O5'_A$	Asp766-OD2	3.2	$O2'_N$	Glu988-OE2	2.8
$O1P_A$	Wat9	2.4	$O4'_N$	Tyr907-OH	2.8
$O2P_A$	Gln763-NE2	3.7			

[a] There are contacts to residues 763, 766, and 770 from the N-terminal domain that have no equivalents in the bacterial toxins *(9)*.

It should be noted that in both known complexes of ARTases with NAD^+ or analogues the so-called "active site loop" becomes labile on NAD^+ binding (*11*, *27*). The equivalent loop of PARP was not used in homology modeling (Figure 6). It consists of residues 881−888 that have low mobility and contact the N-terminal domain of PARP-CF (Figure 1). This correlates well with our failure to bind NAD^+ in the crystals. Furthermore, it agrees with the observation that the random mutant L713F of the N-terminal domain increases the PARP activity by a factor of 9 (*31*), because position 713 is near this loop and is likely to disturb its conformation. Taking these data together, we suggest that the N-terminal domain participates in PARP activity modulation.

Our proposed NAD^+ model is consistent with photolabeling studies demonstrating that 2-azido-NAD^+ (azido group at $C2_A$) labels Lys893 and Trp1014 of human PARP-CF (*32*). Lys893 is located in a loop shielding the adenine moiety of NAD^+ against the solvent (Figure 7).The distance between $C2_A$ and Lys893-O, which had been suggested as the labeled atom (*32*), is 10 Å. The conformation of this loop most likely changes when accommodating the additional azido group such that any atom of Lys893 could come close to $C2_A$, explaining the observed label. Trp1014 is the mobile chain end of PARP-CF that clearly cannot be reached by a 2-azido-NAD^+ molecule bound to the modeled NAD^+ site, because the azido group is buried and at a distance of about 30 Å. Here we suggest that labeling occurs at a subsite of poly(ADP-ribose), which is possible because the photolabel is incorporated in the polymer (*33*). The polymer subsites should be at the surface around the nicotinamide not far from the C-terminus (Figure 2), and it is quite conceivable that the occupant of a subsite can be reached and possibly covered by the mobile Trp1014, explaining its label.

NAD^+ Conformation and Catalysis. A survey of nicotinamide riboses of NAD(P) in the Protein Data Bank yielded 26 independent examples that split nearly equally (11:15) into the two major conformations around 3′-*endo* and around 2′-*endo*, respectively. In the two known cases with ARTases (*11*, *27*), the NMN moiety of NAD^+ binds with a ribose pucker close to 3′-*endo* and the nicotinamide in syn position with angle χ[O4′−C1′−N1−C2] between −20° and +50°. The 3′-*endo* pucker leaves the $C1'_N$ atom well accessible, whereas 2′-*endo* shields it (*11*). In our NAD^+ model we kept the 3′-*endo* pucker of DT:NAD^+.

Presumably, ARTases operate via a transition state with substantial oxocarbenium ion character, similar to the reaction mechanism of inverting glycosidases (*7*, *34*). The oxocarbenium forces the four ribose atoms C2′, C1′, O4′, and C4′ into a plane, which is already assumed in the 3′-*endo* pucker but strongly violated in 2′-*endo*. We therefore suggest that all ARTases bind NAD^+ with the nicotinamide ribose close to the 3′-*endo* pucker and thus close to the transition state, reminiscent of lysozyme binding the reacting pyranose in a suitably deformed conformation.

ACKNOWLEDGMENT

We gratefully acknowledge a gift of the inhibitor NU1025 from D. R. Newell and a gift of PD128763 from Parke-Davis. We thank C. E. Bell and D. Eisenberg for sending us the coordinates of the DT:NAD^+ prior to general distribution. Furthermore, we thank the team of the EMBL outstation, Hamburg, for their support during data collection; A. Pautsch and C. Vonrhein for help in data collection; and V. Rolli for discussions.

REFERENCES

1. Ménissier-de Murcia, J., Niedergang, C., Trucco, C., Ricoul, M., Dutrillaux, B., Mark, M., Oliver, F. J., Masson, M., Dierich, A., LeMeur, M., Walztinger, C., Chambon, P., and de Murcia, G. (1997) *Proc. Natl. Acad. Sci. U.S.A. 94*, 7303−7307.
2. Satoh, M. S., Poirier, G. G., and Lindahl, T. (1994) *Biochemistry 33*, 7099−7106.
3. Farzaneh, F., Meldrum, R., and Shall, S. (1987) *Nucleic Acids Res. 15*, 3493−3502.
4. Realini, C. A., and Althaus, F. R. (1992) *J. Biol. Chem. 267*, 18858−18865.
5. de Murcia, G., and Ménissier de Murcia, J. (1994) *Trends Biochem. Sci. 19*, 172−176.
6. Sebolt-Leopold, J. S., and Scavone, S. V. (1992) *Int. J. Radiat. Oncol., Biol., Phys. 22*, 619−621.
7. Griffin, R. J., Curtin, N. J., Newell, D. R., Golding, B. T., Durkacz, B. W., and Calvert, A. H. (1995) *Biochimie 77*, 408−422.
8. Simonin, F., Höfferer, L., Panzeter, P. L., Muller, S., de Murcia, G., and Althaus, F. R. (1993) *J. Biol. Chem. 268*, 13454−13461.
9. Ruf, A., Ménissier de Murcia, J., de Murcia, G. M., and Schulz, G. E. (1996) *Proc. Natl. Acad. Sci. U.S.A. 93*, 7481−7485.
10. Okazaki, I. J., and Moss, J. (1994) *Mol. Cell. Biochem. 138*, 177−181.
11. Bell, C. E., and Eisenberg, D. (1996) *Biochemistry 35*, 1137−1149.
12. Jung, S., Alves Miranda, E., Ménissier de Murcia, J., Niedergang, C., Delarue, M., Schulz, G. E., and de Murcia, G. (1994) *J. Mol. Biol. 244*, 114−116.
13. Leslie, A. G. W. (1991) in *Crystallographic Computing* (Moras, D., Podjarny, A. D., and Thierry, J. C., Eds.) pp 50−61, Oxford University Press, Oxford.

14. Evans, P. R. (1993) in *Data collection and processing: Proceeedings of the CCP4 study weekend* (Sawyer L., Isaacs N., and Bailey S., Eds.) pp 114−122, SERC Daresbury Laboratory, Warrington, U.K.
15. Otwinowski, Z. (1993) in *Data collection and processing: Proceeedings of the CCP4 study weekend* (Sawyer L., Isaacs N., and Bailey S., Eds.) pp 56−62, SERC Daresbury Laboratory, Warrington, UK.
16. Brünger, A. T. (1992) *X-PLOR*: *A System for X-ray Crystallography and NMR*, Version 3.1, Yale University Press, New Haven, CT.
17. Jiang, J.-S., and Brünger, A. T (1994) *J. Mol. Biol. 243*, 100−115.
18. Kleywegt, G. J. (1995) *ESF/CCP4 Newsletter 31*, pp 45−50, Daresbury, Warrington, U.K.
19. Tripos Associates, Inc. (1992) *SYBYL molecular modeling software*, St. Louis, MO.
20. Brünger, A. T. (1992) *Nature 355*, 472−475.
21. Laskowski, R. A., MacArthur, M. W., Moss, D. S., and Thornton, J. M. (1993) *J. Appl. Crystallogr. 26*, 283−291.
22. Holm, L., and Sander, C. (1993) *J. Mol. Biol. 233*, 123−138.
23. Sixma, T. K., Kalk, K. H., van Zanten, B. A. M., Dauter, Z., Kingma, J., Wiltholt, B., and Hol, W. G. J. (1993) *J. Mol. Biol. 230*, 890−918.
24. Bennett, M. J., Choe, S., and Eisenberg, D. (1994) *Protein Sci. 3*, 1444−1463.
25. Stein, P. E., Boodhoo, A., Armstrong, G. D., Cockle, S. A., Klein, M. H., and Read, R. J. (1994) *Structure 2*, 45−57.
26. Zhang, R.-G., Scott, D. L., Westbrook, M. L., Nance, S., Spangler, B. D., Shipley, G. G., and Westbrook, E. M. (1995) *J. Mol. Biol. 251*, 563−573.
27. Li, M., Dyda, F., Benhar, I., Pastan, I., and Davies, D. R. (1996) *Proc. Natl. Acad. Sci. U.S.A. 93*, 6902−6906.
28. Simonin, F., Ménissier-de Murcia, J., Poch, O., Muller, S., Gradwohl, G., Molinete, M., Penning C., Keith, G., and de Murcia, G. (1990) *J. Biol. Chem. 265*, 19249−19256.
29. Moodie, S. L., and Thornton, J. M. (1993) *Nucleic Acids Res. 21*, 1369−1380.
30. Rolli, V., O'Farrel, M., Ménissier-de Murcia, J., and de Murcia, G. (1997) *Biochemistry 36*, 12147−12154.
31. Alves-Miranda, E., Dantzer, F., O'Farrell, M., de Murcia, G., and Ménissier-de Murcia, J. (1995) *Biochem. Biophys. Res. Commun. 212*, 317−325.
32. Kim, H., Jacobson, M. K., Rolli, V., Ménissier-de Murcia, J., Reinbolt, J., Simonin, F., Ruf, A., Schulz, G. E., and de Murcia, G. (1997) *Biochem. J. 322*, 469−475.
33. Manning, E. L., Kim, H., Haley, B. E., and Jacobson, M. K. (1990) *FASEB J. 4*, A2122, Abstr. 2483.
34. McCarter, J. D., and Withers, S. G. (1994) *Curr. Opin. Struct. Biol. 4*, 885−892.
35. Read, R. J. (1986) *Acta Crytallogr., Sect. A 42*, 140−149.
36. Kraulis, P. J. (1991) *J. Appl. Crystallogr. 24*, 946−950.
37. Suto, M. J., Turner, W. R., Werbel, L. M., Arundel-Suto, C. M., and Sebolt-Leopold, J. S. (1991) *Anticancer Drug Des. 7*, 107−117.
38. Banasik, M. K., and Ueda, K. (1994) *Mol. Cell. Biochem. 138*, 185−197.
39. Boulton, S., Pemberton, L. C., Porteous, J. K., Curtin, N. J., Griffin, R. J., Golding, B. T., and Durkacz, B. W. (1995) *Br. J. Cancer 72*, 849−856.

BI972383S